Global estimates of ambient reactive nitrogen components during 2000-2100 based on the multi-stage model

Rui Li[a, b *], Yining Gao[a], Lijia Zhang[a], Yubing Shen[a], Gehui Wang[a]

[a] *Key Laboratory of Geographic Information Science of the Ministry of Education, School of Geographic Sciences, East China Normal University, Shanghai, 200241, PR China*

[b] *Institute of Eco-Chongming (IEC), 20 Cuiniao Road, Chenjia Town, Chongming District, Shanghai, 202162, China*

* Corresponding author

Prof. Li (rli@geo.ecnu.edu.cn)

Abstract

High contents of reactive nitrogen components aggravate air pollution and could also impact ecosystem structure and function across the terrestrial-aquatic-marine continuum. However, the long-term historical trends and future prediction of reactive nitrogen components at the global scale still remains high uncertainties. In our study, the field observations, satellite products, model output, and many other covariates were integrated into the multi-stage machine-learning model to capture the global patterns of reactive nitrogen components during 2000-2019. In order to decrease the estimate uncertainties in the future scenarios, the constructed reactive nitrogen component dataset during the historical period was then utilized as the constraint to calibrate the CMIP6 dataset in four scenarios. The results suggested the cross-validation (CV) R^2 values of four species showed satisfied performance ($R^2 > 0.55$). The concentrations of estimated reactive nitrogen components in China experienced persistent increases during 2000-2013, while they suffered from drastic decreases since 2013 except NH_3. It might be associated with the impact of clean air policy. However, these compounds in Europe and the United States remained relatively stable since 2000. In the future scenarios, SSP3-7.0 (traditional energy scenario) and SSP1-2.6 (carbon neutrality scenario) showed the highest and lowest reactive nitrogen component concentrations, respectively. Although the reactive nitrogen concentrations in some heavy-pollution scenarios (SSP3-7.0) also experienced decreases during 2020-2100, SSP1-2.6 and SSP2-4.5 (middle emission scenario) still kept more rapid decreasing trends. Our results emphasize the need for carbon-neutrality pathway to reduce global atmospheric N pollution.

1. Introduction

Along with the development of global urbanization and industrialization, the anthropogenic emissions of reactive nitrogen (e.g., NO_x, NH_3, ~~HNO_3~~) experienced drastic increases during the past decades, and caused the higher concentrations of NO_2, NH_3, and many secondary components such as NO_3^- (NO_3-N), NH_4^+ (NH_4-N), and HNO_3 (Chen et al., 2021; Liu et al., 2020b; McDuffie et al., 2020). The reactive nitrogen released from anthropogenic source could significantly alter the global nitrogen cycle throughout the Earth system (Altieri et al., 2021; Zhang et al., 2020). Reactive nitrogen in the atmosphere dominates the chemical formation of tropospheric O_3 and aggravates the particle pollution (Geddes and Martin, 2017), with implications for global air quality and climate change (He et al., 2022; Von Schneidemesser et al., 2015). Moreover, the ambient reactive nitrogen could be deposited into the land surface and could cause lake eutrophication and soil acidification (Bouwman et al., 2002; Chen et al., 2018). Therefore, it is highly necessary to understand the spatial distributions and temporal evolution trends of reactive nitrogen components at the global scale.

Despite the global importance, observational constraints on reactive nitrogen in the atmosphere were still scarce in most parts of the world (Liu et al., 2020b). Furthermore, the majority of monitoring sites focused on China, Europe, and the United States (Du et al., 2014; Li et al., 2020; Li et al., 2019a; Li et al., 2016), and these uneven sites only possessed limited spatial representativeness (Shi et al., 2018), which restricted the accurate assessment of global reactive nitrogen pollution. Fortunately, the satellite observations gave us a unprecedent chance to capture the global variations of atmospheric reactive nitrogen. Geddes et al. (2017) used the satellite products to calibrate the simulated reactive nitrogen oxides (NO_y) and improved the predictive performance (R = 0.83) compared with the chemical transport model (CTM) output alone (Geddes and Martin, 2017). Afterwards, Liu et al. (2022) also used the similar method to estimate the global wet deposition of reduced nitrogen (NH_4^+) and the R value achieved 0.80(Liu et al., 2021). Although the calibration based on satellite products could improve the predictive accuracy compared with CTM output, the simulated values still largely biased from the ground-level observations. Moreover, the method cannot accurately fill the gaps of reactive nitrogen concentrations without satellite coverage. In our previous works, we developed a satellite-based ensemble machine-learning model to predict the wet NH_4^+ deposition across China and the R^2 value reached 0.76 (R = 0.88) (Li et al.,

59 2020). However, this technique was not expanded to the global scale and the high-accuracy and full-

60 coverage global ambient reactive nitrogen dataset was still lack.

61   Apart from the historical estimates, the future prediction of reactive nitrogen is also important

62 because these components in the future scenarios could significantly affect the land carbon cycle

63 and greenhouse gas emissions, both of which could aggravate the global climate change and affect

64 the earth system safety (Chen et al., 2015; Zaehle, 2013). To the best of our knowledge, only two

65 studies focused on global aerosol prediction in the future scenarios. Chen et al. (2023) predicted the

66 global $PM_{2.5}$ levels and associated mortalities in 2100 under different climate scenarios and found

67 that SSP3-7.0 scenario was linked with the highest $PM_{2.5}$ exposure. Li et al., (2022) also simulated

68 the global NO_3^- (NO_3-N) and NH_4^+ (NH_4-N) levels in the future four scenarios and demonstrated

69 that both of these components showed marked decreases in most cases except SSP5-8.5 scenario.

70 However, this study predicted the future reactive nitrogen based on historical CTM output alone,

71 which lacks of observation constraints. The result might increase the uncertainty of assessment.

72   In our study, we developed a multi-stage model to estimate the concentrations of four reactive

73 nitrogen species (NO_3^- (NO_3-N), HNO_3, NH_3, and NH_4^+ (NH_4-N)) during 2000-2019 because these

74 species were most important reactive nitrogen components for human health and ecological

75 ecosystem and also showed abundant ground-level observations. Then, the species over the 2020-

76 2100 period under the SSP1-2.6, SSP2-4.5, SSP3-7.0, and SSP5-8.5 scenarios were also corrected

77 based on the historical estimates. Finally, the long-term dataset of reactive nitrogen during 2000-

78 2100 was constructed. Our results were beneficial to assess the impacts of reactive nitrogen

79 components on air pollution and climate change in the future.

80 **2. Material and methods**

81 2.1 Reactive nitrogen observations

82   Most of reactive nitrogen observations focused on East Asia, Europe, and the United States. The

83 monthly reactive nitrogen components monitoring data during 2010-2015 in China were

84 downloaded from nationwide nitrogen deposition monitoring network (NNDMN) including 32 sites,

85 and these sites could be classified into three types mixed with urban, rural, and background sites

86 (Xu et al., 2019) (Table S1). The concentrations of reactive nitrogen components were determined

87 using the active DEnuder for Long-Term Atmospheric sampling system (DELTA). The detailed

88 sampling and analysis procedures have been described by Xu et al. (2019). The dataset of reactive

89 nitrogen components in other countries of East Asia during 2000-2019 were download from the

90 Acid Deposition Monitoring Network in East Asia (EANET), which includes 41 sites. The European

91 Monitoring and Evaluation Programme (EMEP) provides records of long-term reactive nitrogen

92 components in 86 sites of most countries across West Europe. Monthly reactive nitrogen

93 components dataset in 84 locations across the United States could be obtained from the Clean Air

94 Status and Trends Network (CASTNET) (Figure S1).

95 2.2 Data preparation

96   The GEOS-Chem (v13.4.0) model driven by MERRA2 meteorological parameters was applied

97 to simulate the historical reactive nitrogen components (daily) during 2000-2019 (Feng et al., 2021).

98 The GEOS-Chem model was composed of detailed ozone-NO_x-VOC-PM-halogen tropospheric

99 chemistry. The grid version of the model with a horizontal resolution of $2° \times 2.5°$ was utilized. Wet

100 deposition contained many processes including sub-grid scavenging in convective updrafts, in-

101 cloud rainout, and below-cloud washout (Liu et al., 2001). Dry deposition was estimated based on

102 a resistance-in-series model (Wesely, 2007). The estimates of aerosol optical properties account for

103 the hygroscopic growth (Drury et al., 2010). Vertical mixing in the boundary layer follows a non-

104 local scheme implemented by Lin and McElroy (2010), and convection employs the relaxed

105 Arakawa-Schubert scheme. The anthropogenic emission inventory in 2000-2019 was downloaded

106 from the website of Community Emissions Data System (CEDS) (Hoesly et al., 2018). CEDS

107 emission inventory includes eight sectors such as agriculture, energy, industry, residential, shipping,

108 solvents, transportation, and waste incineration. Then, the daily reactive nitrogen components were

109 averaged to the monthly scale.

110   The IASI instrument aboard on the polar sun-synchronous MetOp platform traverses the

111 equation twice each day (9:30 a.m. and 9:30 p.m. local solar time) (Whitburn et al., 2016a). The

112 measurements in the daytime usually shows the better accuracy than those at night due to the high

113 sensitivity to ambient NH_3 (Van Damme et al., 2017; Whitburn et al., 2016a; Whitburn et al., 2016b).

114 In our study, we used the IASI NH_3 columns in morning during 2008-2019 to estimate the NH_3 and

115 NH_4^+ concentrations globally. Besides, the NH_3 column dataset with a cloud shield higher than 25%

116 and relative error above 100% were eliminated.

The tropospheric vertical column density (VCD) of NO_2 retrieved from OMI aboard on Aura satellite crosses the earth once a day (Kim et al., 2016). OMI-derived tropospheric NO_2 column densities during 2005-2019 was applied to develop the model. The tropospheric NO_2 column density data with cloud radiance fraction > 0.5, terrain reflectivity > 30%, and solar zenith angles > 85° were screened (Cooper et al., 2022). Additionally, the NO_2 columns from GOME (1995-2003), SCIAMACHY (2002-2011) and GOME-2 (2007-) were also collected to simulate the NO_3^- (NO$_3$-N) and HNO_3 levels. The similar overpass time of these three instruments (from about 09:30 to 10:30 LT, local time) facilitates the simultaneous use to capture consistent long-term coverage. However, the dataset cannot cover the NO_2 columns since 2017. To overcome the inconsistency of these satellite products, we applied the linear regression technique to construct the relationship between OMI-NO_2 columns and GOME/SCIAMACHY NO_2 columns. The results suggested these satellite products showed good relationship (R^2 > 0.6). At last, the long-term (2000-2019) NO_2 columns at the global scale were constructed.

The monthly meteorological parameters derived from ERA-5 comprise of 2 m dewpoint temperature (D_{2m}), 2 m temperature (T_{2m}), surface pressure (S_p), and total precipitation (T_p), 10 m U wind component (U10), and 10 m V wind component (V10). The population density data during 2000-2020 around the world were downloaded from https://hub.worldpop.org/geodata/listing?id=64. The elevation data was extracted from ETOPO at a spatial resolution of 1' (Amante and Eakins, 2009) (https://rda.ucar.edu/datasets/ds759.4/). In addition, the land use data types including cropland, forest, grassland, shrubland, tundra, barren land, and snow/ice were obtained from Liu et al. (2020a). Besides, the CMIP6 dataset in four scenarios were also applied to predict the reactive nitrogen concentrations during 2020-2100. The dataset includes 2-m air temperatures, wind speed at 850 and 500 hPa, total cloud cover, precipitation, relative humidity, and short-wave radiation. The modelled meteorological parameters derived from 16 earth system models were incorporated into the machine-learning model. The detailed models are summarized in Table S2.

2.3 Model development

A three-stage model was established to capture the full-coverage reactive nitrogen dataset at the global scale (Figure 1). In the first stage, the ground-level reactive nitrogen species, satellite

146 products (e.g., OMI-NO$_2$ and IASI-NH$_3$ columns), meteorological ~~factors~~parameters, land use types,

147 population, and simulated reactive nitrogen components derived from GEOS-Chem model were

148 collected as the independent variables to estimate the gridded reactive nitrogen species at the

149 period/grid with satellite product based on ~~LightGBM~~ XGBoost algorithm. In the second stage, the

150 meteorological parameters, GEOS-Chem output, land use ~~data~~types, and population were applied

151 to fill the gaps without satellite retrievals. Then, the simulated results based on these models were

152 fused to obtain the full-coverage reactive nitrogen components and the ground-level observations

153 were further used to calibrate the full-coverage dataset and the final reactive nitrogen components

154 at the global scale were simulated. In the last stage, the reactive nitrogen components and

155 meteorological parameters in four scenarios (SSP1-2.6, SSP2-4.5, SSP3-7.0, and SSP5-8.5) during

156 2020-2100 were collected from CMIP6 dataset including 16 earth system models (Table S2). Then,

157 the data in the future scenarios were integrated into the ensemble model including XGBoost,

158 LightGBM, and convolutional neural networks (CNN) to further calibrate the modeling results

159 based on historical dataset (2000-2019) derived from previous two-stage model. The detailed

160 equations of multiple machine-learning models are summarized as follows:

161 (1) XGBoost model

162 $$F^{(t)} = \sum_{i=1}^{n} [l(y_i, \overset{\Lambda}{y}^{(t-1)}) + \partial_{y^{(t-1)}} l(y_i, \overset{\Lambda}{y}^{(t-1)}) f_t(x_i) + \frac{1}{2} \partial_{y^{(t-1)}}^2 l(y_i, \overset{\Lambda}{y}^{(t-1)}) f_t^2(x_i)] + \Omega(f_t) \quad (1)$$

163 where F$^{(t)}$ is the cost function at the t-th period; ∂ is the derivative of the function; $\partial_{y^{(t-1)}}^2$

164 represents the second derivative of the function; l denotes the differentiable convex loss function

165 that reveals the difference of the predicted value ($\overset{\Lambda}{y}$) of the i-th instance at the t-th period and the

166 target value (y$_i$); f$_t$(x) represents the increment; $\Omega(f_t)$ reflects the regularizer. Maximum tree

167 depth and learning rate reached 15 and 0.1, respectively.

168 (2) LightGBM model

169 $$\overset{\Lambda}{f} = \arg\min_f E_{y,X} Q(y, f(x)) \quad (2)$$

170 $$f_T(X) = \sum_{t=1}^{T} f_t(X) \quad (3)$$

171 where Q(y,f(x)) reflects the a specific loss function; $\sum_{t=1}^{T} f_t(X)$ denotes the regression trees.

172 Maximum tree depth, learning rate, and feature fraction reached 25, 0.2, and 0.7, respectively.

173 (3) CNN model

174 The reactive nitrogen species and meteorological parameters in the future scenarios were applied to

175 CNN model based on the historical (2000-2019) reactive nitrogen species derived from stage 1-2

176 model.

177 $$x \xrightarrow{f:U-Net} y \qquad (4)$$

178 where x $(x_1, x_2, \cdots, x_n)$ represents the reactive nitrogen species and meteorological parameters

179 derived from CMIP6 dataset; y $(y_1, y_2, \cdots, y_n)$ denotes the historical (2000-2019) reactive nitrogen

180 species.

181 All of the convolution layers showed the same kernel size of 3×3 and used rectified linear unit

182 (ReLU) as the activation function. Max-pooling layers were employed for adjusting the size of

183 images to capture better bottleneck information. After each block, the image size could be halved

184 by using the max pooling layer with kernel size of 2×2, but the number of channels will be doubled.

185 In our study, the learning rate was set as 0.1 to achieve the best performance.

186 All of the independent variables collected from multiple sources were resampled to 0.25° grids

187 using appropriate algorithmsKriging interpolation. For example, both of the population density and

188 land use types in each grid were calculated using spatial clipping toolbox. Later on, all of these

189 variables were combined to develop the model. During the development of multi-stage model, it

190 was highly imperative to remove some redundant explanatory variables and then determine the

191 optimal variable group. The redundant variables means that the overall predictive accuracy could

192 degrade after the removal of these variables.

193 **3. Results and discussion**

194 3.1 The modelling performance of historical reactive nitrogen estimates

195 The multi-stage model was applied to capture the spatiotemporal variations of reactive nitrogen

196 concentrations during 2000-2100. In our study, we employed XGBoost model to construct the full-

197 coverage reactive nitrogen dataset during 2000-2020. The cross-validation (CV) R^2 values of the

198 model for NO_3^- (NO$_3$-N), HNO_3, NH_3, and NH_4^+ (NH$_4$-N) estimates reached 0.67, 0.62, 0.58, and

199 0.60, respectively (Figure 2). RMSE of NO_3^- (NO₃-N), HNO_3, NH_3, and NH_4^+ (NH₄-N) were 0.55,

200 0.23, 2.32, and 1.71 µg N m⁻³, respectively. MAE of NO_3^- (NO₃-N), HNO_3, NH_3, and NH_4^+ (NH₄-

201 N)~~NO₃⁻, HNO₃, NH₃, and NH₄⁺~~ reached 0.19, 0.13, 1.23, and 0.59 µg N m⁻³. The CV R^2 values of

202 NO_3^- (NO₃-N), HNO_3, and NH_4^+ (NH₄-N) estimates were significantly higher than Jia et al. (2016)

203 (0.22, 0.41, and 0.49), while the CV R^2 value of NO_3^- estimate in our study was comparable to

204 Geddes et al. (2017) (0.68) (Geddes and Martin, 2017). The CV R^2 value of NH_3 estimates were

205 also close to the results obtained by Liu et al. (2019) (0.45-0.71) (Liu et al., 2019). Overall, the

206 predictive performances historical reactive nitrogen was satisfied. Although the CV R^2 values in our

207 study were not significantly higher than those in some previous studies, our study developed the

208 full-coverage (gap-free) ambient reactive nitrogen dataset, which was superior to some previous

209 studies. Based on the constructed full-coverage reactive nitrogen dataset, we also developed the

210 ensemble model to calibrate the CMIP6 dataset in the future scenarios. The CV R^2 values of the

211 model for NO_3^- (NO₃-N), HNO_3, NH_3, and NH_4^+ (NH₄-N)~~NO₃⁻, HNO₃, NH₃, and NH₄⁺~~ estimates in

212 the future scenarios reached 0.62, 0.67, 0.56, and 0.60, respectively (Figure S2). RMSE of NO_3^-

213 (NO₃-N), HNO_3, NH_3, and NH_4^+ (NH₄-N)~~NO₃⁻, HNO₃, NH₃, and NH₄⁺~~ were 0.58, 0.26, 2.12, and

214 1.91 µg N m⁻³, respectively. MAE of NO_3^- (NO₃-N), HNO_3, NH_3, and NH_4^+ (NH₄-N)~~NO₃⁻, HNO₃,~~

215 ~~NH₃, and NH₄⁺~~ reached 0.22, 0.22, 1.04, and 0.65 µg N m⁻³. Overall, the ensemble model for these

216 species in the future scenarios still showed satisfied performance, and thus the result could be treated

217 to be robust.

218 3.2 The spatial patterns of nitrogen reactive components

219 The global annual mean concentrations of NO_3^-, HNO_3, NH_3, and NH_4^+ during 2000-2019

220 ranged from 0.03 to 9.08, 0.03 to 1.73, 0.21 to 13.9, and 0.08 to 17.1 µg N m⁻³ with the mean values

221 of 0.43 ± 0.24 (standard deviation over grids), 0.28 ± 0.13, 1.79 ± 0.85, and 0.65 ± 0.36 µg N m⁻³

222 (Figure S3), respectively. ~~China~~East Asia especially China, West Europe, and the United States

223 obtained widespread attention due to the developed economy and dense anthropogenic activity.

224 In China, the overall mean ambient NO_3^- (NO₃-N), HNO_3, NH_3, and NH_4^+ (NH₄-N)~~NO₃⁻,~~

225 ~~HNO₃, NH₃, and NH₄⁺~~ concentrations reached 1.05 ± 0.62, 0.35 ± 0.19, 4.05 ± 1.84, and 2.38 ± 1.26

226 µg N m⁻³, ranging from 0.07-9.08, 0.06-1.73, 0.84-11.6, and 0.18-13.1 µg N m⁻³. At the regional

227 scale, the annual mean NO_3^-, HNO_3, NH_3, and NH_4^+ concentrations followed the order of North

China Plain (NCP) (4.38, 1.12, 7.22, and 7.69 μg N m^{-3}) > Sichuan Basin (2.40 $\pm$ 1.01, 0.52 $\pm$ 0.28,

4.92 $\pm$ 1.71, and 6.02 $\pm$ 1.82 μg N m^{-3}) (Figure 3). NCP displayed the higher NO$_3^-$ and HNO$_3$

concentrations owing to dense human activities and strong industry foundation (Qi et al., 2023; Wen

et al., 2018), which could emit a large amount of NO$_x$ to the atmosphere. In both of Yangtze River

Delta (YRD) and Pearl River Delta (PRD), the combustion of fossil fuels and traffic emissions might

be the major source of NO$_x$ emission, which aggravated nitrate events via gas-particle conversion

processes (Huang et al., 2017; Li et al., 2017). For Sichuan Basin, the poor topographical or

meteorological conditions were major factors responsible for the severe nitrate pollution (Zhang et

al., 2019). It was not surprising that high ambient NH$_3$ concentrations focused on NCP and Sichuan

Basin because ~~most of Chinese~~many croplands (dry land) are distributed on these regions (Karra et

al., 2021; Potapov et al., 2022), which was the major source of NH$_3$ emissions with frequent N

fertilizer applications (Ma et al., 2022). Besides, N manure was another major source of NH$_3$

emissions in China, and the percentage of N manure to NH$_3$ emissions exceeds 50% (Kang et al.,

2016). The spatial pattern of NH$_4^+$ level was in good agreement with the NH$_3$ concentration because

NH$_4^+$ was often generated from the reaction of NH$_3$ with SO$_2$ and NO$_2$ (Ehrnsperger and Klemm,

2021). Apart from China, many other countries such as South Korea and Japan also showed the

higher ambient reactive nitrogen concentrations. As shown in Figure 3, the higher reactive N

concentrations occurred on the western coasts of South Korea than on the eastern coasts. The higher

reactive N concentrations in Japan mainly focused on the urban areas around Tokyo, which might

be linked with the dense anthropogenic emission in this region (Li et al., 2024). In Southeast Asia,

Indonesia (NO$_3^-$ (NO$_3$-N), HNO$_3$, NH$_3$, and NH$_4^+$ (NH$_4$-N): 0.18, 0.47, 5.72, and 0.44 μg N m^{-3})

suffered from the most serious reactive N pollution compared with other surrounding countries.

In Europe, the ambient NO$_3^-$ (NO$_3$-N), HNO$_3$, NH$_3$, and NH$_4^+$ (NH$_4$-N)~~NO$_3^-$, HNO$_3$, NH$_3$, and NH$_4^+$~~ concentrations ranged from 0.13 to 2.84, 0.06 to 0.92, 0.35 to 7.81, and 0.22 to 3.77 μg N m^{-3}, respectively. The annual mean NO$_3^-$ (NO$_3$-N), HNO$_3$, NH$_3$, and NH$_4^+$ (NH$_4$-N)~~NO$_3^-$, HNO$_3$, NH$_3$, and NH$_4^+$~~ levels reached 0.57 $\pm$ 0.28, 0.25 $\pm$ 0.11, 1.58 $\pm$ 0.68, and 0.89 $\pm$ 0.42 μg N m^{-3}, respectively

(Figure 4). High concentrations of reactive nitrogen components focused on the northern part of

Italy, central and southern part of Germany, North France, Poland, and the western part of Russia,

which was in good agreement with the spatial pattern of NO$_x$ and NH$_3$ emissions (Luo et al., 2022;

Qu et al., 2020). Emissions Database for Global Atmospheric Research (EDGAR) suggested that N fertilization and N manure accounted for 43% and 53% of total NH_3 emissions in western Europe (Liu et al., 2019), respectively. Furthermore, Liu et al. (2019) confirmed that a good relationship between ambient NH_3 level and N fertilization plus N manure (r = 0.62) was observed in Europe. Cooper et al. (2017) employed the inversion model to estimate NO_x emission in Europe and also found that high NO_x emission was also mainly distributed on North France, Germany, the northern part of Italy, and Russia, which partly explained the higher concentrations of reactive nitrogen components in these regions.

In the United States, the ambient NO_3^- (NO_3-N), HNO_3, NH_3, and NH_4^+ (NH_4-N)~~NO_2^-, HNO_3, NH_3, and NH_4^+~~ concentrations reached 0.28 ± 0.12, 0.19 ± 0.08, 2.12 ± 0.66, and 0.49 ± 0.25 µg N m^{-3}, with the range of 0.03-2.35, 0.03-1.31, 0.26-9.96, and 0.10-6.09 µg N m^{-3} (Figure 5), respectively. The hotspots of NO_3^- (NO_3-N)~~NO_2^-~~, HNO_3, and NH_4^+ (NH_4-N) levels focused on the eastern part of the United States, while the higher NH_3 concentration focused on Central Great Plains and some regions in California such as San Joaquin Valley (6.15 µg N m^{-3}). Both of bottom-up and top-down NO_x and NH_3 emissions suggested that the spatial distributions of reactive nitrogen components were strongly dependent on the precursor emissions (McDuffie et al., 2020; Qu et al., 2020).

Besides, some other regions such as India (1.4, 0.5, 6.6, and 4.4 µg N m^{-3}) especially the northern part of India (3.1, 0.8, 12.6, and 8.4 µg N m^{-3}) also experienced severe reactive N pollution in the atmosphere. Meanwhile, some countries in South America such Brazil~~–~~ and Argentina and in Africa such as West Africa Coast (Nigeria, Ivory Coast, Ghana, Togo, and Benin) (HNO_3 and NH_3: 0.3 and 5.0 µg N m^{-3}) and Democratic Congo (0.4 and 1.6 µg N m^{-3}) also suffered from serious HNO_3 (Brazil and Argentina: 0.3 and 0.2 µg N m^{-3}) and NH_3 (3.6 and 2.8 µg N m^{-3}) pollution. The higher ambient NH_3 concentration focused on the northern part of India might be contributed by two major reasons. First of all, the intensive agricultural activities and high air temperature might be responsible for the higher NH_3 level (Cui, 2023; Wang et al., 2020). Moreover, the relatively low sulfur dioxide (SO_2) and nitrogen oxides (NO_x) emissions coupled with high air temperature restricted the gas-to-particle conversion of NH_3 (Wang et al., 2020). The severe HNO_3 and NH_3 pollution in Brazil ~~and~~, Argentina, and West Africa Coast might be also linked with the dense

286 agricultural activities (Huneeus et al., 2017).

287 3.3 The seasonal variations of reactive nitrogen components

288 The ambient NO_3^- (NO_3-N), HNO_3, NH_3, and NH_4^+ (NH_4-N)~~NO_3^-, HNO_3, NH_3, and NH_4^+~~

289 concentrations exhibited significant seasonal variations (Figure S4-8). NO_3^-, HNO_3, and NH_4^+

290 displayed the highest and lowest values in winter (December-February) and summer (June-August),

291 respectively. On the one hand, the anthropogenic NO_x emission for domestic heating might be higher

292 in winter compared with other seasons (Lin et al., 2011). On the other hand, the stagnant

293 meteorological conditions limited the pollutant diffusion (Li et al., 2019b; Liu et al., 2020c).

294 Meanwhile, the higher relative humidity in winter facilitated the formation of NH_4NO_3 (Huang et

295 al., 2016; Xu et al., 2012). However, both of ambient NO_3^- and NH_4^+ concentrations showed the

296 lower concentrations in summer, which might be attributable to the decomposition of NH_4NO_3

297 under the condition of high air temperature. In contrast to the secondary inorganic nitrogen, the

298 ambient NH_3 level showed the highest concentration in summer (1.71 ± 0.45 μg N m^{-3}). China,

299 Europe, and the United States suffered from similar NH_3 peaks in summer (4.20 ± 1.85, 1.77 ± 0.65,

300 and 2.21 ± 1.04 μg N m^{-3}). There are two reasons accounting for the fact. At first, mineral N fertilizer

301 or manure application was mainly performed in spring and early summer (Paulot et al., 2014). Many

302 field observations have obtained similar NH_3 peak in summer (He et al., 2021; Pan et al., 2018).

303 Moreover, summer often showed the higher air temperature, which promotes the volatilization of

304 ammonium and limits the gas-to-particle of gaseous NH_3 (Liu et al., 2019).

305 3.4 The historical trends of reactive nitrogen components during 2000-2019

306 The long-term trends of ambient NO_3^- (NO_3-N), HNO_3, NH_3, and NH_4^+ (NH_4-N)~~NO_3^-, HNO_3,~~

307 ~~NH_3, and NH_4^+~~ concentrations are shown in Figure 6 and Figure S9-12. The NO_3^- concentration in

308 China displayed rapid increase (9.7%/yr) during 2000-2007, and then it kept the moderate increase

309 (4.2%/yr) during 2007-2013. However, the NO_3^- (NO_3-N) concentration in China experienced the

310 drastic decrease (-2.6%/yr) since 2013. The ambient HNO_3 and NH_4^+ (NH_4-N) concentrations

311 showed similar trends during this period. Due to the impact of Clean Air Action, the concentrations

312 of gaseous precursors (e.g., SO_2 and NO_x) suffered from substantial decreases, which could be

313 transformed into nitrate and ammonium via heterogeneous reactions (Huang et al., 2019). However,

314 the decreasing rates of NO_3^- were still much lower than those of gaseous precursors (Li et al., 2023).

On the one hand, it might be associated with the increased O_3 level and enhanced atmospheric oxidation capacity (AOC), which led to an increase in the photochemical reaction rate of the secondary components (Wang et al., 2019). On the other hand, strong SO_2 emission control under the Clean Air Action allowed more gaseous NH_3 to form nitrate. The ambient NH_3 level remained relatively stable status during 2000-2013, while it experienced rapid increases after 2013. The result was in good agreement with Liu et al. (2019). In fact, the ambient NH_3 level in North China Plain still experienced dramatic increase (> 0.2 μg N m^{-3}/yr) during 2000-2013 because enhanced agricultural activities. Zhang et al. (2017) have demonstrated that the livestock manure and fertilizer application generally accounted for 43% and 36% of the agricultural NH_3 emission, respectively. Since 2013, the NH_3 concentration in the entire China suffered from rapid increase, which might be associated with the drastic decrease of sulfate. It was well known that NH_3 could react with HNO_3 and gaseous H_2SO_4 to generate ammonia sulfate and ammonia nitrate (Wang et al., 2022; Wang et al., 2019). Substantial decreases of acidic gases (e.g., SO_2) lead to the reduction of NH_3 conversion to ammonia salts in the atmosphere (Chen et al., 2019), which result in excess NH_3 remaining in the gaseous phase. Different from China, the reactive N concentrations in some other Asia and Africa countries especially India (NO_3^-, HNO_3, NH_3, and NH_4^+: 54%, 46%, 11%, and 94%), South Korea (76%, 42%, 40%, and 9%), Indonesia (21%, 5%, 14%, and 41%), Democratic Congo (9%, 16%, 145%, 41%), and West Africa Coast (4%, 11%, 37%, and 106%) still exhibited stable increases during 2000-2019. The results indicated that no strong reactive N emission control measures were implemented in these countries, which should be further exerted imperatively.

Compared with China, the long-term trends of reactive nitrogen components Europe and the United States were relatively stable. In the Europe, the concentrations of NO_3^- (NO_3-N), HNO_3, and NH_3 exhibited increases during 2000-2007 (0.7%/yr, 2.3%/yr, and 2.1%/yr), while they experienced slight decreases after 2007. The NH_4^+ (NH_4-N) level displayed continuous decrease since 2000. The result was closely linked with the trends of NO_x and NH_3 emissions derived from satellite retrieval (Cooper et al., 2017; Luo et al., 2022). In the United States, both of NO_3^- and NH_4^+ showed persistent decreases during 2000-2019. Zhang et al. (2018) have confirmed that NO_x emission in the eastern US has experienced persistent decrease since 1990, which facilitated the decreases of NO_3^- and NH_4^+ levels. However, the ambient HNO_3 and NH_3 concentrations displayed slight increases during

344 2000-2007 (2.1%/yr), and then remained relatively stable since 2007. Liu et al. (2019) also found

345 similar characteristic of ambient NH_3 trend in the United States. In fact, the NH_3 concentrations in

346 the Middle Plain and eastern US still showed increases due to the lack of NH_3 emission control

347 policies as well as the decline in acidic gases (Warner et al., 2017). The reactive N concentrations

348 in some countries in South America such as Brazil (9%, 0%, 13%, and 34%) and Argentina (10%,

349 12%, 18%, and 7%) also remained relatively stable because local anthropogenic emission of reactive

350 N did not show dramatic increases in the past two decades (McDuffie et al., 2020).

351 3.5 Projection of future ambient reactive nitrogen components

352 For the future reactive nitrogen component estimates, the ensemble model was applied to

353 predict the reactive nitrogen component concentrations under the SSP1-2.6, SSP2-4.5, SSP3-7.0,

354 and SSP5-8.5 scenarios. SSP1-2.6 represents the low emission pathways. In SSP1-2.6, the projected

355 average NO_3^- concentrations in most countries experienced rapid decreases from 2020 to 2100

356 (Figure 7 and Table 1). The mean concentrations of NO_3^- in China, India, Europe, and the United

357 States decreased from 1.16 ± 0.35, 1.23 ± 0.42, 0.41 ± 0.14, and 0.27 ± 0.09 μg N m^{-3} to 0.33 ± 0.10,

358 0.65 ± 0.21, 0.10 ± 0.03, and 0.06 ± 0.02 μg N m^{-3} during 2020-2100 in SSP1-2.6 scenario,

359 respectively. Besides, the NO_3^- concentrations in many other countries of Africa and South America

360 such as Brazil (-127%) and Democratic Congo (-162%) also suffered from drastic decreases in this

361 scenario. SSP2-4.5 scenario represents the middle range of plausible future pathways (Nazarenko

362 et al., 2022). In this scenario, the predicted average NO_3^- concentrations in China, India, Europe,

363 and the United States decreased from 1.19 ± 0.40, 1.43 ± 0.35, 0.44 ± 0.13, and 0.24 ± 0.08 μg N

364 m^{-3} to 0.41 ± 0.14, 0.95 ± 0.32, 0.24 ± 0.08, and 0.05 ± 0.02 μg N m^{-3} during 2020-2100, respectively.

365 SSP3-7.0 and SSP5-8.5 denote the less investment in the environment and heavily relies on

366 traditional energy for rapid economic development, respectively. The ambient NO_3^- in these

367 scenarios generally showed the higher concentrations compared with other scenarios. For instance,

368 the NO_3^- concentrations in China reduced from 1.25 ± 0.40 (SSP3-7.0) and 1.21 ± 0.39 (SSP5-8.5)

369 to 0.75 ± 0.25 (SSP3-7.0) and 0.58 ± 0.18 (SSP5-8.5) μg N m^{-3} during 2020-2100 (Figure 8),

370 respectively. The higher NO_3^- concentrations in SSP3-7.0 and SSP5-8.5 might be associated with

371 the higher anthropogenic NO_x emission. Compard with SSP1-2.6 and SSP2-4.5, the NO_3^-

372 concentrations in some countries during SSP3-7.0 and SSP5-8.5 scenarios displayed slight increases

373 from 2020 to 2040. For instance, the ambient NO_3^- concentrations in Indonesia increased by 12%

374 (SSP3-7.0) and 5% (SSP5-8.5), respectively.

375 The temporal variations of ambient HNO_3 were similar to those of NO_3^- concentrations. The

376 mean concentrations of HNO_3 in China, India, Europe, and the United States decreased from 0.25

377 $\pm$ 0.09, 0.50 $\pm$ 0.16, 0.18 $\pm$ 0.06, and 0.08 $\pm$ 0.03 μg N m^{-3} to 0.05 $\pm$ 0.01, 0.24 $\pm$ 0.08, 0.05 $\pm$ 0.02,

378 and 0.03 $\pm$ 0.01 μg N m^{-3} during 2020-2100 in SSP1-2.6 scenario (Figure S13-S14 and Table S3),

379 respectively. However, the decreasing ratios of ambient HNO_3 levels especially in some developing

380 countries such as Democratic Congo (-13%) and West Africa Coast (-47%) were much less than

381 those of ambient NO_3^- levels. For the SSP3-7.0 and SSP5-8.5 scenarios, the HNO_3 levels in some

382 developing countries such as Democratic Congo (18%), West Africa Coast (16%), Indonesia (13%)

383 even experienced moderate increases. It was assumed that the government gave less investment in

384 environment improvement and the anthropogenic emission did not show marked decrease under the

385 condition of SSP3-7.0 scenario (Chen et al., 2023; Chen et al., 2020).

386 As shown in Figure S15-S18 and Table S4-S5, the higher ambient NH_3 and NH_4^+

387 concentrations also focused on India and North China. In SSP1-2.6, the ambient NH_3 (NH_4^+)

388 concentrations in China, India, Europe, and the United States decreased from 3.51 $\pm$ 1.12 (2.00 $\pm$

389 0.62), 6.30 $\pm$ 2.12 (4.26 $\pm$ 1.42), 1.54 $\pm$ 0.51 (0.75 $\pm$ 0.24), and 1.79 $\pm$ 0.59 (0.53 $\pm$ 0.17) μg N m^{-3}

390 to 1.75 $\pm$ 0.58 (0.58 $\pm$ 0.19), 2.57 $\pm$ 0.85 (1.25 $\pm$ 0.41), 1.15 $\pm$ 0.36 (0.50 $\pm$ 0.16), and 1.58 $\pm$ 0.52

391 (0.45 $\pm$ 0.15) μg N m^{-3} during 2020-2100. Compared with SSP1-2.6, the ambient NH_3 and NH_4^+

392 concentrations in heavy-pollution scenarios (SSP3-7.0, and SSP5-8.5) scenarios did not show

393 marked decreases from 2020-2100. Some developing countries such as Argentina (9%), Democratic

394 Congo (25%), and West Africa Coast (24%) even suffered from persistent increases of ambient NH_3

395 and NH_4^+ levels. It might be associated with ineffective control of NH_3 emission compared with

396 NO_x emission.

397 3.6 ~~Implications~~ Conclusions and limitations

398 The ground-level ambient reactive nitrogen observations, satellite retrievals, GEOS-Chem

399 model output, and many other geographical covariates were integrated into the multi-stage model

400 to reveal the global patterns of ambient reactive nitrogen components during 2000-2019. Then, these

401 high-resolution reactive nitrogen dataset during the historical period was then utilized as the

带格式的: 缩进: 首行缩进: 2 字符

constraint to calibrate the CMIP6 dataset in four scenarios during 2020-2100. The results indicated the cross-validation (CV) R^2 values of four reactive nitrogen species showed satisfied performance ($R^2 > 0.55$). At the spatial scale, four reactive nitrogen components exhibited the higher concentrations in China and India. For the temporal variations, the concentrations of estimated ambient reactive nitrogen components in China experienced persistent increases during 2000-2013, while they suffered from drastic decreases since 2013 except NH_3, which might be linked with the impact of clean air policy. However, the concentrations of these species in Europe and the United States remained relatively stable since 2000. In the future scenarios, SSP3-7.0 (traditional energy scenario) and SSP1-2.6 (carbon neutrality scenario) displayed the highest and lowest reactive nitrogen component concentrations, respectively.

Global trends of four reactive nitrogen components during 2000-2100 emphasizes the urgent mitigation measures (carbon neutrality pathway) to reduce precursor emissions in order to decrease the concentrations and depositions of reactive nitrogen components especially in China and India. Furthermore, our result could give valuable insights into the impact of reactive nitrogen components on human health and ecological environment. However, this study still shows some limitations. First of all, the observation networks mainly focus on China, Europe, and the United States, and thus the simulations in many other regions might show large uncertainties. Secondly, both of the GEOS-Chem output and CMIP6 future climate scenario data also exhibits large uncertainties, which could impact the reliability of this study. Lastly, our predictions were performed on the basis of the premise that the world was steadily developing, and cannot predict the impacts of uncontrollable factors (e.g., COVID-19, Russia-Ukraine War).

Competing interests

The contact author has declared that none of the authors has any competing interests.

Acknowledgements

This work was supported by the National Natural Science Foundation of China (U23A2030).

Data availability

The CMIP6 dataset used in this publication is available in https://esgf.nci.org.au/projects/cmip6-nci/.

Author contributions

431   LR and WGH designed the study; LR developed the model; GYN, ZLJ, and SYB analyzed the

432   observation and model data. LR wrote this manuscript.

433

434 **Figure 1** The workflow of global full-coverage reactive nitrogen estimates during 2000-2100.
435 GC_{output} denotes the GEOS-Chem output.
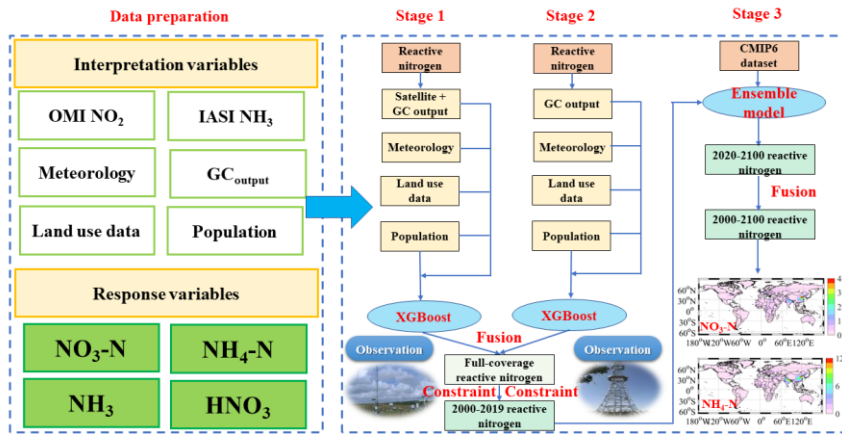
436

437 **Figure 2** The predictive performances of four reactive nitrogen components including NO_3^- (a),
438   HNO_3 (b), NH_3 (c), and NH_4^+ (d). The model was constructed with 90% original data and the
439   remained data was applied to validate the model. The black solid line denotes the best-fitting curve
440   for all of the points, while the black dashed line represents the diagonal, which means the same
441   observed and simulated values. The color scale denotes the sample size.
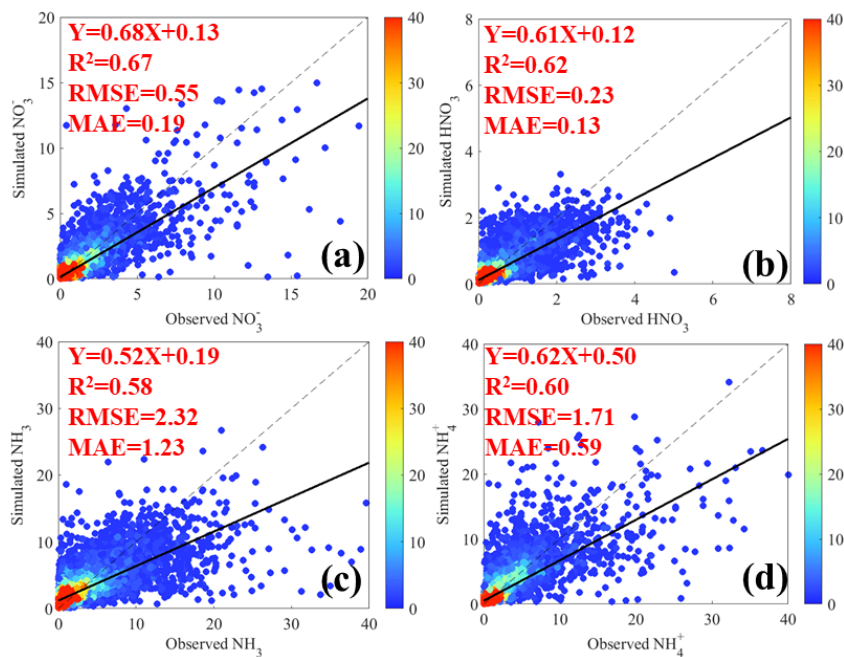
442

443 **Figure 3** The spatiotemporal variations of NO_3^-, HNO_3, NH_3, and NH_4^+ concentrations in East Asia

444 (a-d) (Unit: μg N m^{-3}).
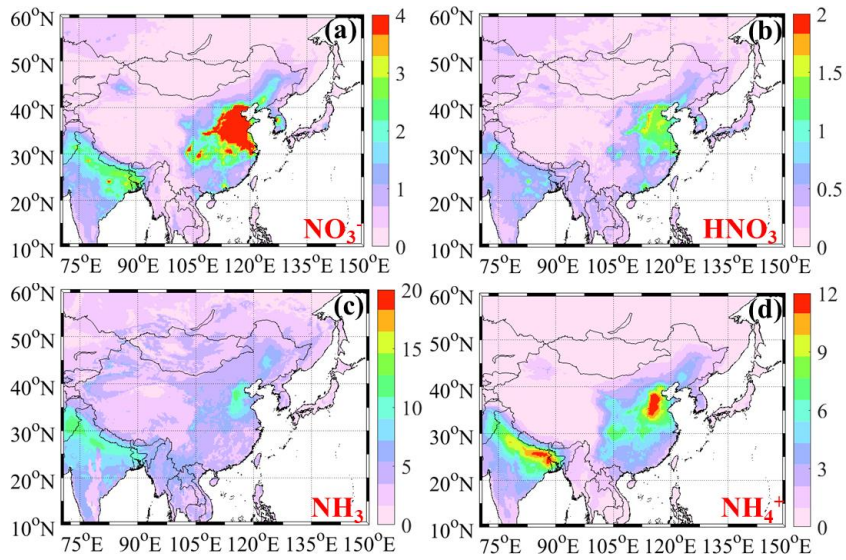
445

446

447 **Figure 4** The spatiotemporal variations of NO_3^-, HNO_3, NH_3, and NH_4^+ concentrations in Europe

448 (a-d) (Unit: $\mu g\ N\ m^{-3}$).
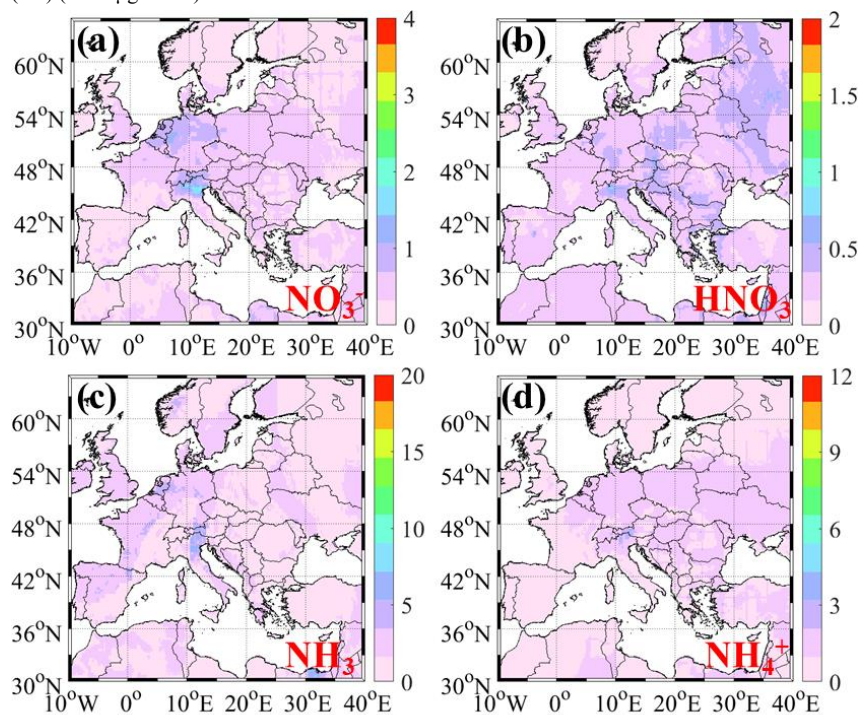
449
450

451 **Figure 5** The spatiotemporal variations of NO_3^-, HNO_3, NH_3, and NH_4^+ concentrations in North
452 America (a-d) (Unit: μg N m^{-3}).
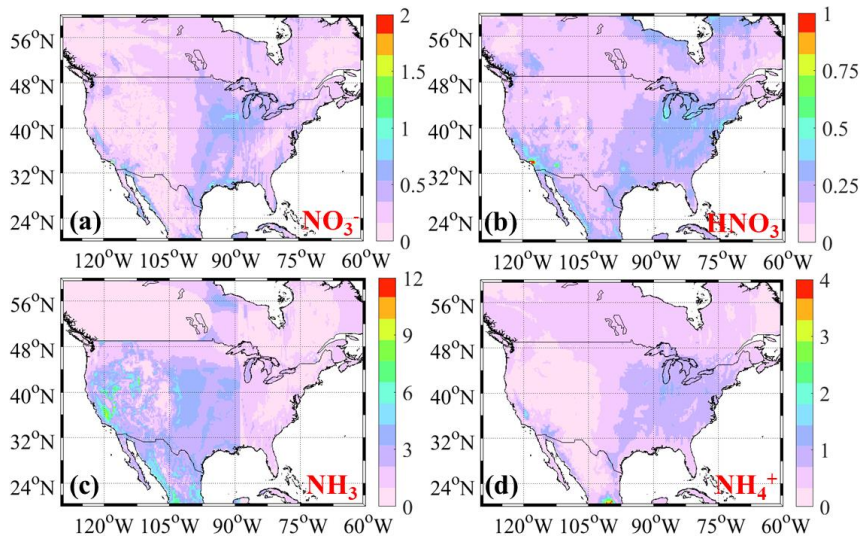
453

454 **Figure 6** The long-term variations of NO_3^-, HNO_3, NH_3, and NH_4^+ concentrations in China (pink),
455 Europe (green), and the United States (cyan) (Unit: µg N m^{-3}).

456
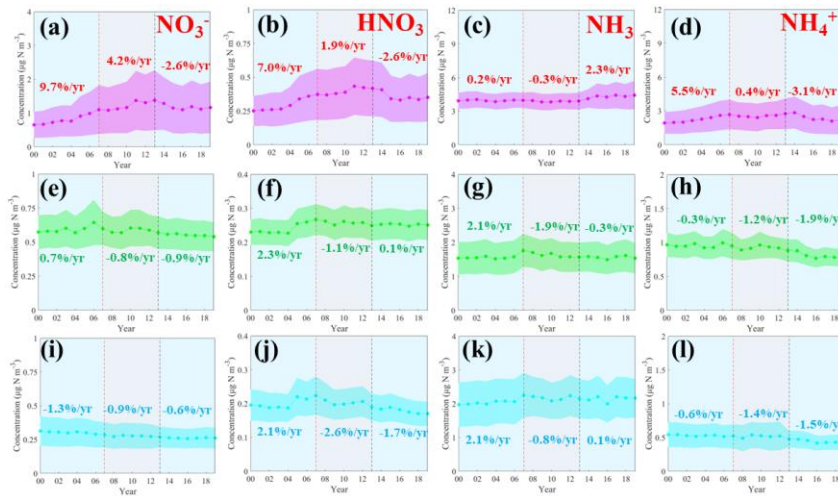
Figure 7 Spatial variations of projected global ambient concentrations of reactive nitrogen components under different climate change scenarios (Unit: μg N m^{-3}). Panels (a-b) represent the annual mean concentrations of ambient NO$_3^-$ under SSP1-2.6, SSP2-4.5 during 2021-2100, respectively.
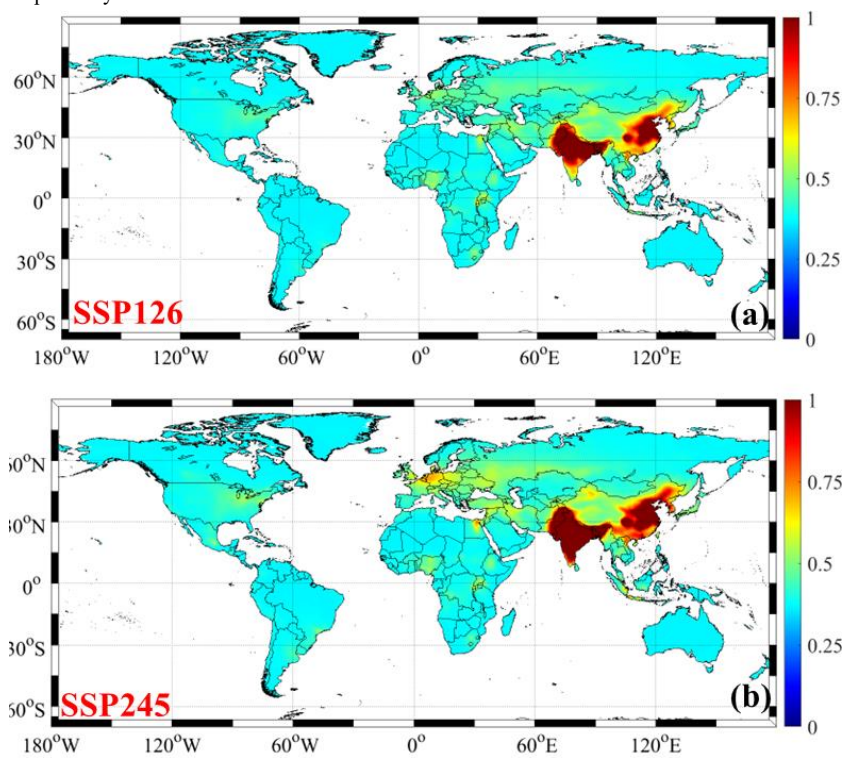
Figure 8 Spatial variations of projected global ambient concentrations of reactive nitrogen components under different climate change scenarios (Unit: µg N m^{-3}). Panels (a-b) represent the annual mean concentrations of ambient NO$_3^-$ under SSP3-7.0, and SSP5-8.5 during 2021-2100, respectively.
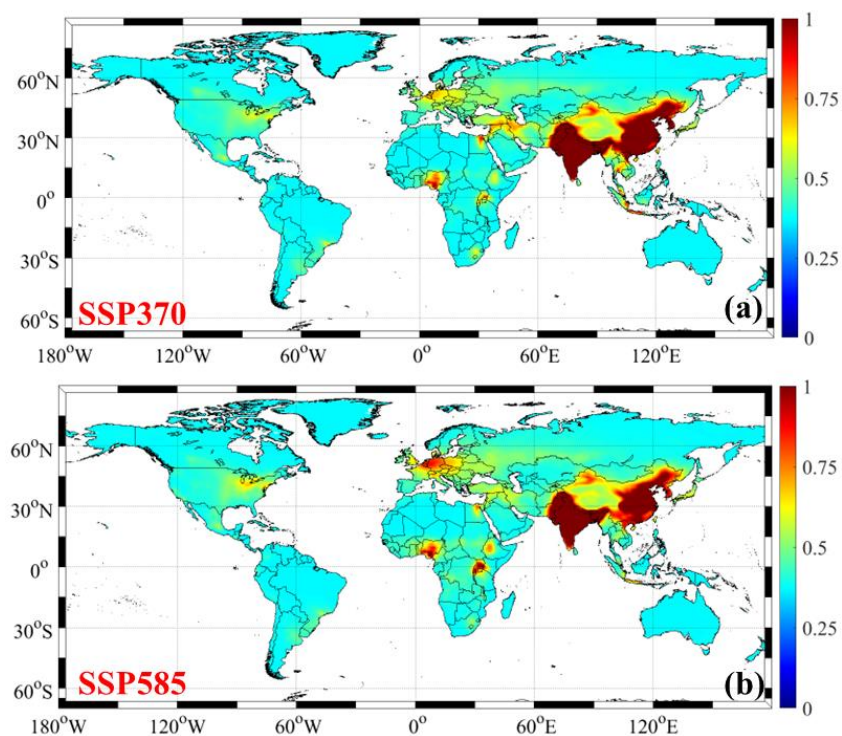
469 **Table 1** The temporal variations of ambient NO_3^- (NO_3-N) concentrations (average concentrations)
470 in many countries during 2000-2100.

Scenario	NO_3^-	China	India	Europe	United States	Brazil	Argentina	Democratic Congo	West Africa Coast	Indonesia	South Korea
Historical	2000	0.66	0.95	0.57	0.31	0.29	0.21	0.56	0.30	0.31	1.06
	2005	0.91	1.26	0.60	0.30	0.31	0.22	0.56	0.30	0.34	1.38
	2010	1.17	1.53	0.60	0.28	0.33	0.23	0.58	0.31	0.32	1.43
	2013	1.39	1.63	0.57	0.27	0.30	0.24	0.58	0.31	0.33	1.57
	2015	1.16	1.34	0.56	0.26	0.32	0.22	0.58	0.32	0.45	1.88
	2019	1.18	1.46	0.54	0.26	0.32	0.23	0.61	0.32	0.37	1.87
SSP1-2.6	2020	1.16	1.23	0.41	0.27	0.25	0.18	0.55	0.28	0.34	1.81
	2040	0.82	1.12	0.28	0.10	0.21	0.14	0.62	0.32	0.28	1.46
	2060	0.69	1.01	0.15	0.05	0.18	0.13	0.43	0.25	0.24	0.69
	2080	0.41	0.89	0.12	0.05	0.17	0.12	0.32	0.17	0.20	0.39
	2100	0.33	0.65	0.10	0.06	0.11	0.08	0.21	0.11	0.16	0.23
SSP2-4.5	2020	1.19	1.43	0.44	0.24	0.26	0.19	0.52	0.29	0.37	1.85
	2040	1.09	1.35	0.43	0.16	0.22	0.16	0.57	0.31	0.35	1.80
	2060	0.89	1.22	0.35	0.11	0.20	0.15	0.51	0.27	0.32	1.25
	2080	0.63	1.06	0.29	0.07	0.17	0.12	0.42	0.23	0.23	0.68
	2100	0.41	0.95	0.24	0.05	0.14	0.10	0.36	0.19	0.20	0.38
SSP3-7.0	2020	1.25	1.59	0.53	0.33	0.31	0.22	0.64	0.34	0.42	1.95
	2040	1.36	1.50	0.47	0.24	0.26	0.19	0.61	0.33	0.47	1.89
	2060	1.18	1.35	0.42	0.19	0.22	0.16	0.56	0.30	0.41	1.56
	2080	0.96	1.15	0.36	0.16	0.18	0.13	0.54	0.29	0.35	1.35
	2100	0.75	1.08	0.33	0.12	0.15	0.11	0.51	0.27	0.30	1.24
SSP5-8.5	2020	1.21	1.50	0.53	0.28	0.28	0.20	0.57	0.31	0.37	1.91
	2040	1.28	1.42	0.49	0.23	0.25	0.18	0.60	0.32	0.39	1.85
	2060	1.05	1.30	0.47	0.24	0.20	0.15	0.55	0.29	0.35	1.44
	2080	0.86	1.10	0.44	0.25	0.15	0.11	0.50	0.27	0.29	1.26
	2100	0.58	1.02	0.31	0.20	0.13	0.09	0.46	0.25	0.25	1.05

471

References

Altieri, K.E., Fawcett, S.E., Hastings, M.G. (2021) Reactive nitrogen cycling in the atmosphere and ocean. Annual Review of Earth and Planetary Sciences 49, 523-550.

Amante, C., Eakins, B.W. (2009) ETOPO1 arc-minute global relief model: procedures, data sources and analysis.

Bouwman, A., Van Vuuren, D., Derwent, R., Posch, M. (2002) A global analysis of acidification and eutrophication of terrestrial ecosystems. Water, Air, and Soil Pollution 141, 349-382.

Chen, H., Li, D., Gurmesa, G.A., Yu, G., Li, L., Zhang, W., Fang, H., Mo, J. (2015) Effects of nitrogen deposition on carbon cycle in terrestrial ecosystems of China: A meta-analysis. Environmental pollution 206, 352-360.

Chen, W., Lu, X., Yuan, D., Chen, Y., Li, Z., Huang, Y., Fung, T., Sun, H., Fung, J.C. (2023) Global PM2. 5 Prediction and Associated Mortality to 2100 under Different Climate Change Scenarios. Environmental science & technology 57, 10039-10052.

Chen, X., Wang, Y.-h., Ye, C., Zhou, W., Cai, Z.-c., Yang, H., Han, X. (2018) Atmospheric nitrogen deposition associated with the eutrophication of Taihu Lake. Journal of Chemistry 2018.

Chen, Y., Liu, A., Cheng, X. (2020) Quantifying economic impacts of climate change under nine future emission scenarios within CMIP6. Science of the Total Environment 703, 134950.

Chen, Y., Shen, H., Russell, A.G. (2019) Current and future responses of aerosol pH and composition in the US to declining SO_2 emissions and increasing NH3 emissions. Environmental science & technology 53, 9646-9655.

Chen, Y., Zhang, L., Henze, D.K., Zhao, Y., Lu, X., Winiwarter, W., Guo, Y., Liu, X., Wen, Z., Pan, Y. (2021) Interannual variation of reactive nitrogen emissions and their impacts on PM2. 5 air pollution in China during 2005–2015. Environmental Research Letters 16, 125004.

Cooper, M., Martin, R.V., Padmanabhan, A., Henze, D.K. (2017) Comparing mass balance and adjoint methods for inverse modeling of nitrogen dioxide columns for global nitrogen oxide emissions. Journal of Geophysical Research: Atmospheres 122, 4718-4734.

Cooper, M.J., Martin, R.V., Hammer, M.S., Levelt, P.F., Veefkind, P., Lamsal, L.N., Krotkov, N.A., Brook, J.R., McLinden, C.A. (2022) Global fine-scale changes in ambient NO_2 during COVID-19 lockdowns. Nature 601, 380-387.

Cui, L. (2023) Impact of COVID-19 restrictions on the concentration and source apportionment of atmospheric ammonia (NH_3) across India. Science of the Total Environment 881, 163443.

Drury, E., Jacob, D.J., Spurr, R.J.D., Wang, J., Shinozuka, Y., Anderson, B.E., Clarke, A.D., Dibb, J., McNaughton, C. Weber, D., Synthesis of satellite (MODIS), aircraft (ICARTT), and surface (IMPROVE, EPA-AQS, AERONET) aerosol observations over eastern North America to improve MODIS aerosol retrievals and constrain surface aerosol concentrations and sources J. Geophys. Res. Atmos., 115 (2010), p. D14204.

Du, E., de Vries, W., Galloway, J.N., Hu, X., Fang, J. (2014) Changes in wet nitrogen deposition in the United States between 1985 and 2012. Environmental Research Letters 9, 095004.

Ehrnsperger, L., Klemm, O. (2021) Source apportionment of urban ammonia and its contribution to secondary particle formation in a Mid-size European City. Aerosol and Air Quality Research 21, 200404.

Feng, X., Lin, H., Fu, T.-M., Sulprizio, M.P., Zhuang, J., Jacob, D.J., Tian, H., Ma, Y., Zhang, L., Wang, X. (2021) WRF-GC (v2. 0): online two-way coupling of WRF (v3. 9.1. 1) and GEOS-Chem (v12. 7.2) for modeling regional atmospheric chemistry–meteorology interactions. Geoscientific Model

516   Development 14, 3741-3768.

517 Geddes, J.A., Martin, R.V. (2017a) Global deposition of total reactive nitrogen oxides from 1996 to 2014

518   constrained with satellite observations of NO_2 columns. Atmos. Chem. Phys. 17, 10071-10091.

519 He, Y., Pan, Y., Gu, M., Sun, Q., Zhang, Q., Zhang, R., Wang, Y. (2021) Changes of ammonia

520   concentrations in wintertime on the North China Plain from 2018 to 2020. Atmospheric Research 253,

521   105490.

522 He, Z., Liu, P., Zhao, X., He, X., Liu, J., Mu, Y. (2022) Responses of surface O3 and PM2. 5 trends to

523   changes of anthropogenic emissions in summer over Beijing during 2014–2019: A study based on

524   multiple linear regression and WRF-Chem. Science of the Total Environment 807, 150792.

525 Hoesly, R.M., Smith, S.J., Feng, L., Klimont, Z., Janssens-Maenhout, G., Pitkanen, T., Seibert, J.J., Vu,

526   L., Andres, R.J., Bolt, R.M. (2018) Historical (1750–2014) anthropogenic emissions of reactive gases

527   and aerosols from the Community Emissions Data System (CEDS). Geoscientific Model Development

528   11, 369-408.

529 Huang, L., An, J., Koo, B., Yarwood, G., Yan, R., Wang, Y., Huang, C., Li, L. (2019) Sulfate formation

530   during heavy winter haze events and the potential contribution from heterogeneous SO 2+ NO 2

531   reactions in the Yangtze River Delta region, China. Atmospheric Chemistry and Physics 19, 14311-

532   14328.

533 Huang, T., Chen, J., Zhao, W., Cheng, J., Cheng, S. (2016) Seasonal variations and correlation analysis

534   of water-soluble inorganic ions in PM2. 5 in Wuhan, 2013. Atmosphere 7, 49.

535 Huang, X., Liu, Z., Liu, J., Hu, B., Wen, T., Tang, G., Zhang, J., Wu, F., Ji, D., Wang, L. (2017) Chemical

536   characterization and source identification of PM 2.5 at multiple sites in the Beijing–Tianjin–Hebei

537   region, China. Atmospheric Chemistry and Physics 17, 12941-12962.

538 Huneeus, N., Granier, C., Dawidowski, L., van Der Gon, H.D., Alonso, M., Castesana, P., Diaz, M., Frost,

539   G.J., Gallardo, L., Gomez, D., (2017) Anthropogenic emissions in South America for air quality and

540   climate modelling, 2017 International Emission Inventory Conference "Applying Science and

541   Streamlining Processes to Improve Inventories".

542 Kang, Y., Liu, M., Song, Y., Huang, X., Yao, H., Cai, X., Zhang, H., Kang, L., Liu, X., Yan, X. (2016)

543   High-resolution ammonia emissions inventories in China from 1980 to 2012. Atmospheric Chemistry

544   and Physics 16, 2043-2058.

545 Karra, K., Kontgis, C., Statman-Weil, Z., Mazzariello, J.C., Mathis, M., Brumby, S.P., (2021) Global

546   land use/land cover with Sentinel 2 and deep learning, 2021 IEEE international geoscience and remote

547   sensing symposium IGARSS. IEEE, pp. 4704-4707.

548 Kim, H.C., Lee, P., Judd, L., Pan, L., Lefer, B. (2016) OMI NO 2 column densities over North American

549   urban cities: the effect of satellite footprint resolution. Geoscientific Model Development 9, 1111-1123.

550 Li, H., Yang, Y., Wang, H., Wang, P., Yue, X., Liao, H. (2022) Projected aerosol changes driven by

551   emissions and climate change using a machine learning method. Environmental science & technology

552   56, 3884-3893.

553 Li, H., Zhang, Q., Zhang, Q., Chen, C., Wang, L., Wei, Z., Zhou, S., Parworth, C., Zheng, B., Canonaco,

554   F. (2017) Wintertime aerosol chemistry and haze evolution in an extremely polluted city of the North

555   China Plain: significant contribution from coal and biomass combustion. Atmospheric Chemistry and

556   Physics 17, 4751-4768.

557 Li, M.; Kurokawa, J.; Zhang, Q.; Woo, J.-H.; Morikawa, T.; Chatani, S.; Lu, Z.; Song, Y.; Geng, G.; Hu,

558   H., MIXv2: a long-term mosaic emission inventory for Asia (2010-2017). Atmospheric Chemistry and

559   Physics 2024, 24, (7), 3925-3952.

Li, R., Cui, L., Fu, H., Zhao, Y., Zhou, W., Chen, J. (2020) Satellite-Based Estimates of Wet Ammonium (NH_4-N) Deposition Fluxes Across China during 2011–2016 Using a Space–Time Ensemble Model. Environmental science & technology 54, 13419-13428.

Li, R., Cui, L., Zhao, Y., Zhang, Z., Sun, T., Li, J., Zhou, W., Meng, Y., Huang, K., Fu, H. (2019a) Wet deposition of inorganic ions in 320 cities across China: spatio-temporal variation, source apportionment, and dominant factors. Atmospheric Chemistry and Physics 19, 11043-11070.

Li, R., Gao, Y., Xu, J., Cui, L., Wang, G. (2023) Impact of Clean Air Policy on Criteria Air Pollutants and Health Risks Across China During 2013–2021. Journal of Geophysical Research: Atmospheres 128, e2023JD038939.

Li, R., Wang, Z., Cui, L., Fu, H., Zhang, L., Kong, L., Chen, W., Chen, J. (2019b) Air pollution characteristics in China during 2015–2016: Spatiotemporal variations and key meteorological factors. Science of the Total Environment 648, 902-915.

Li, Y., Schichtel, B.A., Walker, J.T., Schwede, D.B., Chen, X., Lehmann, C.M., Puchalski, M.A., Gay, D.A., Collett Jr, J.L. (2016) Increasing importance of deposition of reduced nitrogen in the United States. Proceedings of the National Academy of Sciences 113, 5874-5879.

Lin, J.T., McElroy, M.B., (2010) Impacts of boundary layer mixing on pollutant vertical profiles in the lower troposphere: implications to satellite remote sensing Atmos. Environ., 44, pp. 1726-1739.

Lin, W., Xu, X., Ge, B., Liu, X. (2011) Gaseous pollutants in Beijing urban area during the heating period 2007–2008: variability, sources, meteorological, and chemical impacts. Atmospheric Chemistry and Physics 11, 8157-8170.

Liu, H., Gong, P., Wang, J., Clinton, N., Bai, Y., Liang, S. (2020a) Annual dynamics of global land cover and its long-term changes from 1982 to 2015. Earth System Science Data 12, 1217-1243.

Liu, H., Jacob, D.J., Bey, I., Yantosca, R.M. (2001) Constraints from 210Pb and 7Be on wet deposition and transport in a global three-dimensional chemical tracer model driven by assimilated meteorological fields. Journal of Geophysical Research: Atmospheres 106, 12109-12128.

Liu, L., Yang, Y., Xi, R., Zhang, X., Xu, W., Liu, X., Li, Y., Liu, P., Wang, Z. (2021) Global Wet-Reduced Nitrogen Deposition Derived From Combining Satellite Measurements With Output From a Chemistry Transport Model. Journal of Geophysical Research: Atmospheres 126, e2020JD033977.

Liu, L., Zhang, X., Wong, A.Y., Xu, W., Liu, X., Li, Y., Mi, H., Lu, X., Zhao, L., Wang, Z. (2019) Estimating global surface ammonia concentrations inferred from satellite retrievals. Atmospheric Chemistry and Physics 19, 12051-12066.

Liu, L., Zhang, X., Xu, W., Liu, X., Lu, X., Wei, J., Li, Y., Yang, Y., Wang, Z., Wong, A.Y. (2020b) Reviewing global estimates of surface reactive nitrogen concentration and deposition using satellite retrievals. Atmospheric Chemistry and Physics 20, 8641-8658.

Liu, Y., Zhou, Y., Lu, J. (2020c) Exploring the relationship between air pollution and meteorological conditions in China under environmental governance. Scientific reports 10, 14518.

Luo, Z., Zhang, Y., Chen, W., Van Damme, M., Coheur, P.-F., Clarisse, L. (2022) Estimating global ammonia (NH_3) emissions based on IASI observations from 2008 to 2018. Atmospheric Chemistry and Physics 22, 10375-10388.

Ma, R., Yu, K., Xiao, S., Liu, S., Ciais, P., Zou, J. (2022) Data-driven estimates of fertilizer-induced soil NH_3, NO and N_2O emissions from croplands in China and their climate change impacts. Global Change Biology 28, 1008-1022.

McDuffie, E.E., Smith, S.J., O'Rourke, P., Tibrewal, K., Venkataraman, C., Marais, E.A., Zheng, B., Crippa, M., Brauer, M., Martin, R.V. (2020) A global anthropogenic emission inventory of atmospheric

604   pollutants from sector-and fuel-specific sources (1970–2017): an application of the Community
605   Emissions Data System (CEDS). Earth System Science Data 12, 3413-3442.

606 Nazarenko, L.S., Tausnev, N., Russell, G.L., Rind, D., Miller, R.L., Schmidt, G.A., Bauer, S.E., Kelley,
607   M., Ruedy, R., Ackerman, A.S. (2022) Future climate change under SSP emission scenarios with
608   GISS-E2. 1. Journal of Advances in Modeling Earth Systems 14, e2021MS002871.

609 Pan, Y., Tian, S., Zhao, Y., Zhang, L., Zhu, X., Gao, J., Huang, W., Zhou, Y., Song, Y., Zhang, Q. (2018)
610   Identifying ammonia hotspots in China using a national observation network. Environmental science
611   & technology 52, 3926-3934.

612 Paulot, F., Jacob, D.J., Pinder, R., Bash, J., Travis, K., Henze, D. (2014) Ammonia emissions in the
613   United States, European Union, and China derived by high-resolution inversion of ammonium wet
614   deposition data: Interpretation with a new agricultural emissions inventory (MASAGE_NH3). Journal
615   of Geophysical Research: Atmospheres 119, 4343-4364.

616 Potapov, P., Hansen, M.C., Pickens, A., Hernandez-Serna, A., Tyukavina, A., Turubanova, S., Zalles, V.,
617   Li, X., Khan, A., Stolle, F. (2022) The global 2000-2020 land cover and land use change dataset
618   derived from the Landsat archive: first results. Frontiers in Remote Sensing 3, 856903.

619 Qi, L., Zheng, H., Ding, D., Wang, S. (2023) Responses of sulfate and nitrate to anthropogenic emission
620   changes in eastern China-in perspective of long-term variations. Science of the Total Environment 855,
621   158875.

622 Qu, Z., Henze, D.K., Cooper, O.R., Neu, J.L. (2020) Impacts of global NO x inversions on NO 2 and
623   ozone simulations. Atmospheric Chemistry and Physics 20, 13109-13130.

624 Shi, X., Zhao, C., Jiang, J.H., Wang, C., Yang, X., Yung, Y.L. (2018) Spatial representativeness of $PM_{2.5}$
625   concentrations obtained using observations from network stations. Journal of Geophysical Research:
626   Atmospheres 123, 3145-3158.

627 Van Damme, M., Whitburn, S., Clarisse, L., Clerbaux, C., Hurtmans, D., Coheur, P.-F. (2017) Version 2
628   of the IASI NH_3 neural network retrieval algorithm: near-real-time and reanalysed datasets.
629   Atmospheric Measurement Techniques 10, 4905-4914.

630 Von Schneidemesser, E., Monks, P.S., Allan, J.D., Bruhwiler, L., Forster, P., Fowler, D., Lauer, A.,
631   Morgan, W.T., Paasonen, P., Righi, M. (2015) Chemistry and the linkages between air quality and
632   climate change. Chemical reviews 115, 3856-3897.

633 Wang, M., Xiao, M., Bertozzi, B., Marie, G., Rörup, B., Schulze, B., Bardakov, R., He, X.-C., Shen, J.,
634   Scholz, W. (2022) Synergistic HNO_3-H_2SO_4-NH_3 upper tropospheric particle formation. Nature 605,
635   483-489.

636 Wang, T., Song, Y., Xu, Z., Liu, M., Xu, T., Liao, W., Yin, L., Cai, X., Kang, L., Zhang, H., Zhu, T. (2020)
637   Why is the Indo-Gangetic Plain the region with the largest NH3 column in the globe during pre-
638   monsoon and monsoon seasons? Atmos. Chem. Phys. 20, 8727-8736.

639 Wang, Y., Li, W., Gao, W., Liu, Z., Tian, S., Shen, R., Ji, D., Wang, S., Wang, L., Tang, G. (2019) Trends
640   in particulate matter and its chemical compositions in China from 2013–2017. Science China Earth
641   Sciences 62, 1857-1871.

642 Warner, J., Dickerson, R., Wei, Z., Strow, L.L., Wang, Y., Liang, Q. (2017) Increased atmospheric
643   ammonia over the world's major agricultural areas detected from space. Geophysical Research Letters
644   44, 2875-2884.

645 Wen, L., Xue, L., Wang, X., Xu, C., Chen, T., Yang, L., Wang, T., Zhang, Q., Wang, W. (2018)
646   Summertime fine particulate nitrate pollution in the North China Plain: increasing trends, formation
647   mechanisms and implications for control policy. Atmospheric Chemistry and Physics 18, 11261-11275.

648   Wesely, M. (2007) Parameterization of surface resistances to gaseous dry deposition in regional-scale
649   numerical models. Atmospheric Environment 41, 52-63.
650   Whitburn, S., Van Damme, M., Clarisse, L., Bauduin, S., Heald, C., Hadji-Lazaro, J., Hurtmans, D.,
651   Zondlo, M.A., Clerbaux, C., Coheur, P.F. (2016a) A flexible and robust neural network IASI-NH3
652   retrieval algorithm. Journal of Geophysical Research: Atmospheres 121, 6581-6599.
653   Whitburn, S., Van Damme, M., Clarisse, L., Turquety, S., Clerbaux, C., Coheur, P.F. (2016b) Doubling
654   of annual ammonia emissions from the peat fires in Indonesia during the 2015 El Niño. Geophysical
655   Research Letters 43, 11,007-011,014.
656   Xu, L., Chen, X., Chen, J., Zhang, F., He, C., Zhao, J., Yin, L. (2012) Seasonal variations and chemical
657   compositions of $PM_{2.5}$ aerosol in the urban area of Fuzhou, China. Atmospheric Research 104, 264-
658   272.
659   Xu, W., Zhang, L., Liu, X. (2019) A database of atmospheric nitrogen concentration and deposition from
660   the nationwide monitoring network in China. Scientific data 6, 1-6.
661   Zaehle, S. (2013) Terrestrial nitrogen–carbon cycle interactions at the global scale. Philosophical
662   Transactions of the Royal Society B: Biological Sciences 368, 20130125.
663   Zhang, L., Guo, X., Zhao, T., Gong, S., Xu, X., Li, Y., Luo, L., Gui, K., Wang, H., Zheng, Y. (2019) A
664   modelling study of the terrain effects on haze pollution in the Sichuan Basin. Atmospheric
665   Environment 196, 77-85.
666   Zhang, X., Ward, B.B., Sigman, D.M. (2020) Global nitrogen cycle: critical enzymes, organisms, and
667   processes for nitrogen budgets and dynamics. Chemical reviews 120, 5308-5351.
668   Zhang, X., Wu, Y., Liu, X., Reis, S., Jin, J., Dragosits, U., Van Damme, M., Clarisse, L., Whitburn, S.,
669   Coheur, P.-F. (2017) Ammonia emissions may be substantially underestimated in China.
670   Environmental science & technology 51, 12089-12096.
671   Zhang, Y., Mathur, R., Bash, J.O., Hogrefe, C., Xing, J., Roselle, S.J. (2018) Long-term trends in total
672   inorganic nitrogen and sulfur deposition in the US from 1990 to 2010. Atmospheric Chemistry and
673   Physics 18, 9091-9106.
674
675